Molecular orbital imaging beyond the first monolayer: Insights into the pentacene/Ag(110) interface

M. Grimm,[1] C. Metzger,[1] M. Graus,[1] M. Jugovac,[2] G. Zamborlini,[2] V. Feyer,[2] A. Schöll,[1] and F. Reinert[1]
[1]*University of Würzburg, Experimental Physics VII, 97074 Würzburg, Germany*
[2]*Forschungszentrum Jülich GmbH, Peter Grünberg Institute (PGI-6), 52425 Jülich, Germany*

(Received 19 April 2018; revised manuscript received 26 September 2018; published 9 November 2018)

Understanding the molecular geometry at interfaces is not only of importance for optimizing contact properties but also sets the basis in energy alignment in multilayer samples. Here we present a method to determine the tilt angle of molecular compounds by a combination of the orbital imaging technique with photoemission matrix element calculations. By simulating different tilt angles of isolated molecules and comparing the resulting photoemission intensity distribution with momentum maps measured on molecular multilayers, one is able to determine the molecules' tilt angles for each separate layer independently from one another.

DOI: 10.1103/PhysRevB.98.195412

I. INTRODUCTION

Interfaces between organic materials and metals are of crucial importance for applications, e.g., in optoelectronic devices [1–3]. The structural arrangement of the molecular film in the immediate vicinity of the metal is decisive for the relevant contact properties such as the alignment of energy levels at the interface [4–9] or the growth mode of the active organic layer [8,10]. To systematically investigate such contacts, model systems like ordered molecular layers on single crystalline metal surfaces have been employed and probed by several established surface science tools, amongst them photoelectron spectroscopy (PES), low-energy electron diffraction (LEED), near-edge x-ray absorption fine structure (NEXAFS), or scanning tunneling microscopy (STM). Most of these techniques are highly surface sensitive and have provided comprehensive insight into the properties of single adsorbed layers. However, once the interfacial layer in direct contact with the metal is buried by subsequent layers, the former cannot be probed straightforwardly since the applied methods are either too surface sensitive (as STM) or can only hardly distinguish the molecules in the various layers (as NEXAFS). The desired properties of the interface in a more realistic scenario are consequently often not accessible. Here we show on the example of bilayer samples of pentacene on Ag(110) surfaces that by analyzing the angle-resolved PES data along the orbital imaging approach, we can determine the inclination angle, which corresponds to the angle between the normal of the molecular plane and the surface normal of molecules in the topmost as well as in the interfacial layer with very high accuracy. Thus we are able to follow changes of the structural arrangement of the molecules at the interface, which are induced by the growth of additional layers.

II. METHODS

A. Experimental Details

Experiments were done at the NanoESCA beamline of the Elettra synchrotron in Trieste, equipped with an electrostatic photoemission electron microscope (PEEM) [11]. The setup includes a PEEM column and a double-pass hemispherical analyzer. The instrument, in momentum mode operation, can detect momentum maps in the range of $k_{||} \in [-1.8; 1.8]$ 1/Å. Photon energies of 30 eV, 40 eV, and 50 eV were utilized with p-polarization of the incoming light. The Ag(110) substrate was cleaned by repeated cycles of sputtering and annealing. The pentacene (purity 99%, purchased from Sigma-Aldrich) was deposited from a homemade evaporator, which was degased thoroughly prior to sample preparation. The temperature of the evaporator was set to $T = 185\,^{\circ}$C, which resulted in a depostion rate of 25 min per monolayer, as calibrated by XPS and the characteristic LEED signature of the pentacene monolayer/Ag(110) [12]. The sample was kept at room temperature during preparation and LEED experiments, but was cooled down to 140 K for all PES measurements, resulting in an overall energy resolution of about 70 meV.

Figure 1(a) shows the LEED pattern of 1 ML pentacene on Ag(110) with a commensurate superstructure matrix of (3 −1/ −1 4) marked in red. The molecules are aligned along the [001] direction of the Ag(110) substrate, which was also reported in literature [12]. A sketch of the molecular orientation together with the experimental geometry is illustrated in Fig. 2. This sample was prepared by deposition of roughly 2 ML with subsequent tempering at a sample temperature of $T = 180\,^{\circ}$C for 10 min, to remove all molecules from higher layers. The resulted coverage defines what we refer to as ML. Due to significant differences in both LEED and valence band spectra between ML and bilayer (BL) samples [compare with Fig. 1(b)], one can easily verify the success of the applied procedure. So far, we couldn't identify any differences between a tempered ML sample and one with direct evaporation. In Fig. 1(b), we show the LEED pattern of the BL preparation, which was produced by direct evaporation for 45 min at $T = 185\,^{\circ}$C. The red dots still mark the unaltered reflexes known from the ML sample, which proves that additional molecules grow in a second layer and not in a denser ML, with therefore different adsorption geometry. In green we model the additional superstructure with the matrix (5 2/ −2 3) of the second layer.

Figure 1(c) shows the valence regime spectra of both samples investigated in this work measured with an excitation energy of $h\nu = 30$ eV. The first peak close to the Fermi

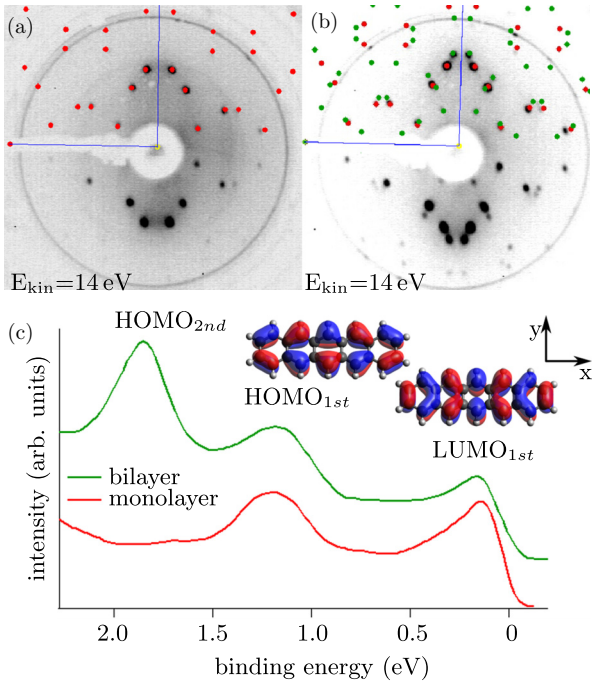

FIG. 1. (a) LEED pattern of 1 ML Pentacene on Ag(110) with simulated superstructure (3 −1/ −1 4) (red). (b) LEED pattern of 1 BL Pentacene on Ag(110) with simulated ML superstructure (3 −1/−1 4) (red) and additional structure of second layer (5 2/ −2 3) (green). c) EDC measured with an excitation energy of $h\nu = 30$ eV and integrated over an area marked in Fig. 3(a). DFT calculation of HOMO and LUMO of isolated pentacene with positive/negative phase illustrated in red/blue.

level originates from the lowest unoccupied molecular orbital (LUMO) of the isolated molecule, which is filled due to charge transfer from the substrate upon adsorption [13–15]. The second peak at a binding energy of $E_{bin} = 1.2$ eV stems from the highest occupied molecular orbital of the first layer (HOMO$_{1st}$), which is in direct contact to the substrate. In contrast, the HOMO of the second layer (BL-HOMO$_{2nd}$) is shifted to $E_{bin} = 1.8$ eV and the LUMO of the molecules in the second layer is not occupied, due to the weaker interaction with the metal substrate, which is screened by the first layer. Both energy distribution curves (EDC) were taken at the

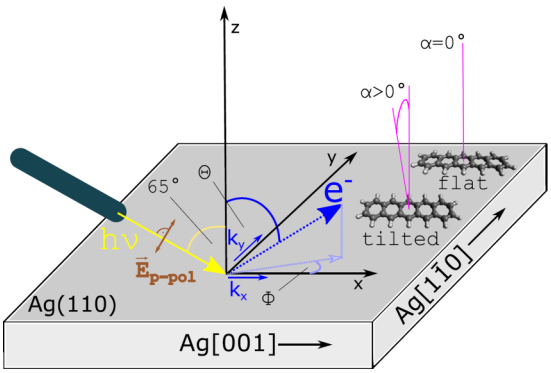

FIG. 2. Illustrated geometry of the measurement process. Two schematically included molecules in the top right indicate the direction of the tilt angle α.

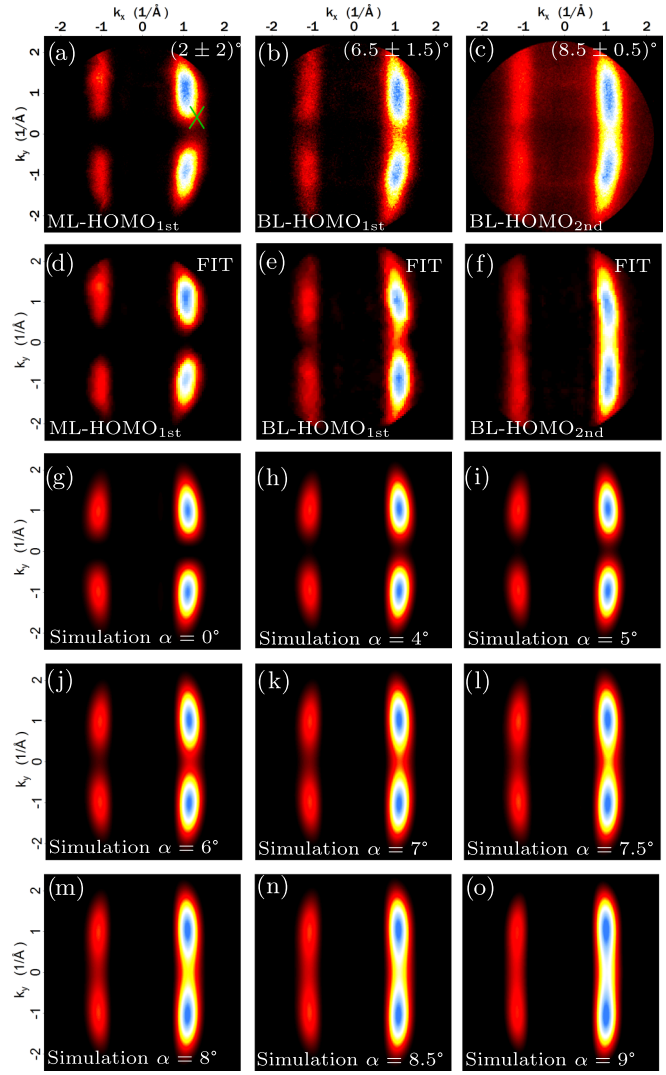

FIG. 3. (a)–(c) Experimental momentum maps derived for the HOMO signals of the first and second layer recorded with an excitation energy of $h\nu = 30$ eV. The green X marks the area in k the EDC from Fig. 1 was taken at. (d)–(f) Momentum maps derived from the fit of the area of the respective HOMO peaks. (g)–(o) IAC-calculations for different tilt angles of the pentacene molecule.

marked point in $k_{||}$, shown in Fig. 3(a) for the ML-HOMO$_{1st}$. The point in momentum space was chosen such that all three molecular states discussed in this report are partially overlapping in $k_{||}$ and thus have finite spectral weight. A closer look at the symmetries of these so-called momentum maps, shown in Fig. 3, allows the identification of different molecular orbitals [16]. In the case of the HOMO, for example, the gas-phase real space DFT-orbital has an antisymmetry plane at $y = 0$ [Fig. 1(c)]. This leads to a suppression of signal and therefore a nodal plane at $k_y = 0$ [see Fig. 3(a)]. The opposite is true for the LUMO. In that case, the symmetry plane at $y = 0$ possesses even parity, which leads to a nonvanishing signal at $k_y = 0$ (see Fig. 5). To attain the experimental momentum maps presented in Fig. 3 second row, the raw data was corrected for screen deficiencies (dark/bright field) and for the nonisochromaticity effect [17–19]. Furthermore, the scaling in $k_{||}$ was achieved by fitting a parabola with an additional

term to the power of 4 to the photoemission onset to minimize distortion due to spherical abberation of the PEEM. No symmetrization of measured data was applied. The light incidence was at an angle of $(65 \pm 5)°$ to the sample normal from negative x direction (see Fig. 2). This leads to a reduction of molecular signals for negative values of k_x with p-polarized light.

B. Photoemission Calculations

For a more accurate assessment of the mechanism governing the detected photoemission spectra, we performed simulations of the photoemission process. We calculated the matrix elements of Fermi's golden rule with initial states based on the linear combination of atomic orbitals and final states with the independent atomic center approximation (IAC), similar to methods already present in literature [20–22]. The photoemission intensity $I_n(\vec{k})$ at wave vector $\vec{k}$ originating from molecular orbital n can therefore be described as the superposition of all atomic contributions:

$$I_n(\vec{k}) \propto \left| \sum_a \langle \psi_{i,a} | \vec{\epsilon} \cdot \vec{r} | \psi_{f,a} \rangle \right|^2, \tag{1}$$

with the interaction operator $\vec{\epsilon} \cdot \vec{r}$ and the partial initial and final states $\psi_{i,a}$ and $\psi_{f,a}$ at atom a, respectively.

The initial state is determined by a DFT calculation on an isolated molecule using Gaussian 09W [23] with a 6-31G+ basis set and the B3LYP functional [24,25]. The final state is constructed from the coherent superposition of partial final states $\psi_{f,a}$ at each atomic site a

$$\psi_{f,a} = 4\pi \sum_{l=0}^{\infty} \sum_{m=-l}^{l} (-1)^l j_l(kr) Y_{l,m}(\hat{r}) Y^*_{l,m}(\hat{k}) \times D_a(k) \delta^l_a(k) e^{-i\vec{k}\vec{R}_a}, \tag{2}$$

with spherical Bessel functions j_l, spherical harmonics $Y_{l,m}$, inelastic damping D_a, and phase shift δ^l_a from the potential of the emitting atom a. The interaction operator is taken from the known geometry and light polarization in the experiment.

III. RESULTS AND DISCUSSION

To test the accuracy of this theoretical approach for such molecular thin film samples, we start by comparing the experimental and simulated momentum maps of the three HOMO (ML-HOMO$_{1st}$, BL-HOMO$_{1st}$, and BL-HOMO$_{2nd}$) similar to Refs. [26–28].

Figure 3(a) represents the experimental momentum map of the HOMO of 1 ML pentacene evaporated on Ag(110) recorded with a photon energy of $h\nu = 30\,\text{eV}$. The nodal plane at $k_y = 0$, caused by the antisymmetry of the real space orbital along $y = 0$, can be clearly observed. The strong forward/backward asymmetry along the k_x direction results from the experimental geometry (compare Fig. 2), where the intensity in the momentum map is generally (excluding some exceptions, e.g., Ref. [29]) modulated by the angle between the vector potential of the incoming radiation and the direction of the photoemitted electron [30]. If a second pentacene layer is added, the pattern of the HOMO of the first layer starts to change and some intensity emerges especially in the former nodal plane at $k_y = 0$ [Fig. 3(b)]. This increased intensity along $k_y = 0$ is even more pronounced for the HOMO of the second layer [Fig. 3(c)]. In this case, the most prominent signals, which are oval shaped in the case of Fig. 3(a), smear out along k_y leading to a vanishing of the nodal plain. The linear color code of all momentum maps was manually set in such a way that the highest intensity is shown in blue and the ratio between signals at positive/negative k_x is kept constant. This ratio is based on the above-mentioned experimental geometry reasons and, therefore, the same (constant) for all measurements. In this representation, the unstructured background, which mainly stems from scattered substrate electrons, is almost completely out of the applied color scale range and therefore suppressed. In contrast to that, the known structure of the bare Ag(110) bands is still partially visible in the experimental data [e.g., Fig. 3(c) or Figs. 4(b) and 4(c)]. Further details about the applied background treatment are given in the Appendix.

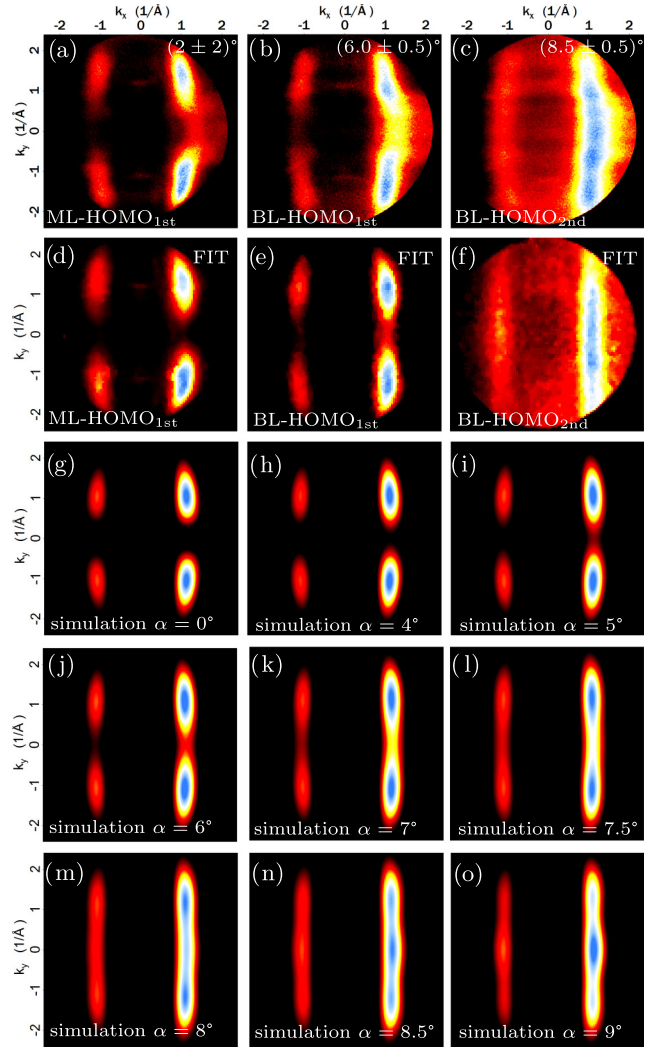

FIG. 4. (a)–(c) Experimental momentum maps derived for the HOMO signals of the first and second layer recorded with an excitation energy of $h\nu = 50\,\text{eV}$. (d)–(f) Momentum maps derived from the fit of the area of the respective HOMO peaks. (g)–(o) IAC-calculations for different tilt angles of the pentacene molecule.

The observed smearing of intensity along k_y can straightforwardly be explained by an inclination of the pentacene molecules in the adsorbate layer, which are tilted against the substrate surface along the long molecular axis [30,31]. Further mechanisms, which are able to change the pattern of the momentum maps like vibrations [32] or band dispersion [15], that have already been reported for similar systems, can not explain this behavior. In case of the present experimental geometry, a tilt angle of $+\alpha$ will lead to an intensity shift towards more positive k_y. Due to the symmetry of the adsorbate system, a mirror domain with a tilt of $-\alpha$ will exist with the corresponding intensity shift toward more negative k_y. To quantify the tilt angle through this effect, momentum maps were simulated with the calculation scheme presented above for isolated molecules of varying tilt angles α between 0° and 9° and summed up for the + and − case, respectively. The results are displayed in Figs. 3(g)–3(o). In general, the simulations reproduce the merging of the prominent oval shaped intensity features along k_y well for increasing angle α. A more detailed comparison of the experimental momentum maps for the three HOMO in Figs. 3(a)–3(c) and the theory results allows a quantification of the tilt angles of the molecules in the respective layers.

For the ML-HOMO$_{1st}$ in Fig. 3(a), a best match between experiment and theory is achieved for an angle $\alpha = (2 \pm 2)°$. Since at such small tilt angles, the intensity features are only slightly elongated but do not overlap significantly, angles between 0° and 4° can hardly be distinguished. The situation is different for the BL-HOMO$_{1st}$ [Fig. 3(b)]. In this case, significant intensity occurs at $k_y = 0$ in between the intensity maxima. To reproduce this observation, a tilt angle of at least $\alpha = 5°$ is required in the simulation. Furthermore, an upper limit for α of 8°, can be derived, since for larger tilt angles the smearing of intensity obviously becomes too strong. We can thus quantify the tilt angle derived for BL-HOMO$_{1st}$ to $\alpha = (6.5 \pm 1.5)°$. Along the same line, the tilt angle for BL-HOMO$_{2nd}$ [Fig. 3(c)] can be determined to $\alpha = (8.5 \pm 0.5)°$.

A possible source of error is the influence of the dispersive bands of the Ag substrate. These can contribute to the intensity patterns and increase the intensity in the regime between the most prominent pentacene features, which is the decisive criterion for the analysis described above. Note that spurious intensity in this regime would immediately result in a larger tilt angle in our evaluation. To minimize this effect, we applied a fitting routine to the three-dimensional data set (k_x, k_y, and E_{bin}) by separating each point in $k_{||}$ into a single EDC (see Appendix Fig. 7 for more details), in which the shape of the main peaks is sufficiently well described by a Gaussian. Therefore the fitting function used for each of the 100 x 100 EDC consists out of one Gaussian for the signal of each molecular orbital, an exponential background from the substrate, all of which were multiplied by a Fermi function and added with a constant offset due to the energy independent background. To remove single points, at which the fit did not converge properly, a denoising routine was applied at the end. Figures 3(d)–3(f) display the resulting area of the respective Gaussian functions plotted against $k_{||}$. The background from the substrate is effectively reduced by this evaluation. However, the differences to the momentum maps in Figs. 3(a)–3(c) are relatively small, which implies that the substrate has only minor influence for our analysis at the chosen photon energy of $h\nu = 30$ eV.

TABLE I. Tilt angles of different HOMO for 30 eV, 40 eV, and 50 eV photon energies.

	α ($h\nu = 30$ eV)	α ($h\nu = 40$ eV)	α ($h\nu = 50$ eV)
ML-HOMO$_{1st}$	$(2 \pm 2)°$	$(2 \pm 2)°$	$(2 \pm 2)°$
BL-HOMO$_{1st}$	$(6.5 \pm 1.5)°$	$(5 \pm 1)°$	$(6.0 \pm 0.5)°$
BL-HOMO$_{2nd}$	$(8.5 \pm 0.5)°$	$(8.5 \pm 0.5)°$	$(8.5 \pm 0.5)°$

The accuracy of the determined tilt angle can be further improved by experiments at larger photon energies. Due to the fixed tilt angle of the molecules, the displacement in k_y of the characteristic molecular intensity features is enhanced at the thus larger k_z. To make use of this effect, we recorded additional data sets at $h\nu = 40$ eV and $h\nu = 50$ eV. Figure 4 shows the experimental and simulated momentum maps for $h\nu = 50$ eV. Here the simulated data shows a much larger effect upon increase of the tilt angle than before in the $h\nu = 30$ eV case. For example, at 9° the two maxima are merged completely, resulting in a new maximum at $k_y = 0$. At the same time, the ratio of molecule-to-substrate signal is significantly decreased, since the maximum photoemission cross section for the C 2p-derived states of pentacene is below $h\nu = 35$ eV [33] in comparison to the maximum cross section of Ag 5s at around $h\nu = 40$ eV [34,35]. Consequently, evaluating α with high accuracy from the as-measured data is complicated and the fitting routine to reduce the background from the substrate becomes mandatory. This is illustrated by the respective results in Figs. 4(d)–4(f). From the comparison of the fit results with the simulation, the tilt angles can be determined to be $\alpha = (2 \pm 2)°$ for the ML-HOMO$_{1st}$, $\alpha = (6.0 \pm 0.5)°$ for the BL-HOMO$_{1st}$, and $\alpha = (8.5 \pm 0.5)°$ for the BL-HOMO$_{2nd}$. These values coincide within their accuracy with the previous results derived from the experiments at $h\nu = 30$ eV.

Table I summarizes all tilt angles for the different HOMO versus different excitation energies and includes also the results of the $h\nu = 40$ eV evaluation, which was done analogously but is not presented here.

So far, only the HOMO was utilized to analyze the tilting behavior of the pentacene molecules in the bilayer sample. In principle, this approach can be applied to any orbital. Figure 5 shows the momentum maps recorded for the LUMO at $h\nu = 30$ eV. Here the most prominent intensity pattern consists of only one oval-shaped feature around $k_y = 0$, with two weaker side lobes at larger absolute k_y. If the LUMO of the ML [Fig. 5(a)] and BL [Fig. 5(b)] are compared, no significant difference is obvious. The simulations in Figs. 5(c)–5(e) show that the main intensity feature is elongated along k_y for larger tilt angles and finally overlaps with the side lobes at 8.5° [Fig. 5(e)]. In contrast to the simulations, this effect can hardly be detected in the experimental momentum maps, from which we can state an upper limit for the tilt angle of $\alpha \leqslant 8.0°$ for the LUMO of the ML and BL sample. From the evaluation of the LUMO, we can state that due to the lack of the discernible features associated with the two molecules with different tilt

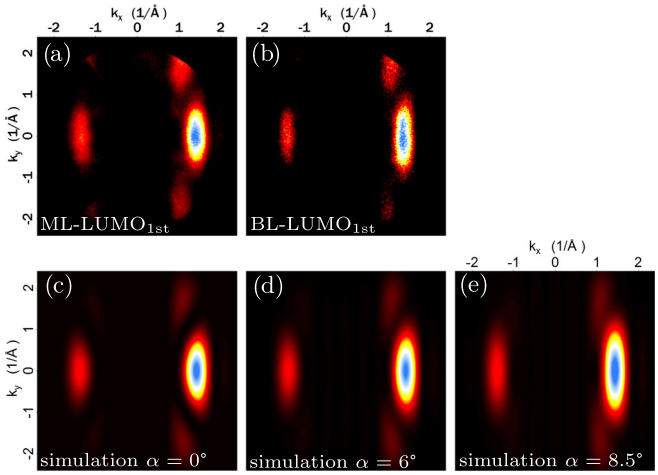

FIG. 5. (a)–(b) Experimental momentum maps of both different LUMO discussed in this report with an excitation energy of $h\nu = 30$ eV. (c)–(e) IAC calculations for different tilt angles of the pentacene molecule.

direction as they occur for the HOMO, the exact tilt angles can be much less exactly derived from the LUMO data. However, the tilt angles derived from the HOMO coincide with the estimation from the LUMO.

This finding is interesting since it shows that not only the molecules in the second layer show a tilt of the pentacene plane of about 8.5° with respect to the substrate surface, but also the first layer, in the case of the bilayer sample, tilts about 6.0° due to the change of the surrounding chemical potential, while the molecules are flat lying in case of a mere monolayer sample. The interfacial layer is thus already significantly altered by the initial growth of the bulk phase, which cannot be investigated selectively in the here presented accuracy with any other surface-sensitive technique (e.g., NEXAFS [36] or STM [37]).

IV. SUMMARY AND CONCLUSION

In summary, we have demonstrated a method to determine the tilt angle of molecular compounds by combining the orbital imaging technique with IAC calculations. By the described approach, we are able to measure the tilt angles of molecules in individual layers independently even for samples consisting of multiple layers. In the discussed example of bilayer samples of pentacene on Ag(110), this is demonstrated for the molecules in the first and in the second layer. However, the application to thicker films is generally only limited by the electron mean free path and a distinguishable spread in energy of the signals originating from the investigated layers, to clearly assign the respective pattern in momentum space. The accuracy of the resulting tilt angles depends on the particular PES spectra, which should show well-distinguishable signals for the different layers of interest, and can be very high, if the momentum maps show sharp intensity features. This is particularly the case for organic aromatic compounds, as demonstrated in the present case for the HOMO of pentacene.

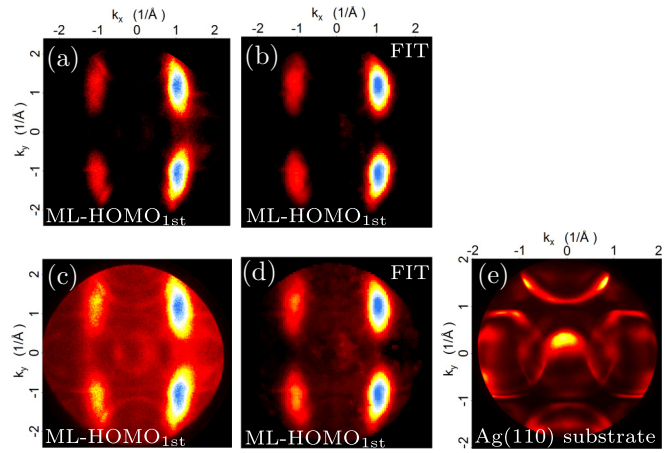

FIG. 6. (a) Experimental momentum map derived for the HOMO signal of the ML sample recorded with an excitation energy of $h\nu = 40$ eV. (b) Momentum map derived from the fit of the area of the HOMO peak, both in the color code used above. (c), (d) Same as in (a) and (b) but with the complete signal of the low-intensity color scale visible. (e) Experimental momentum map of the clean Ag(110) substrate at the same energy as (a)–(d) but with incoming light from the bottom.

ACKNOWLEDGMENTS

We thank Bernd Engels for a fruitful discussion and the Deutsche Forschungsgemeinschaft for funding under Contracts No. SCHO1260/5-1, No. SCHO1260/4-2, and No. SCHO1260/6-1.

APPENDIX

Background removal and fitting routine

The presented experimental data was compared to photoemission calculations for an isolated molecule, thus the Ag-substrate is not considered. The substrate contributes to the experimental signal by the distinct Ag sp-bands as well as by an unstructured signal from inelastically scattered electrons. To account for this and to reduce the signal from the substrate, we applied a fitting routine to the measured data and presented

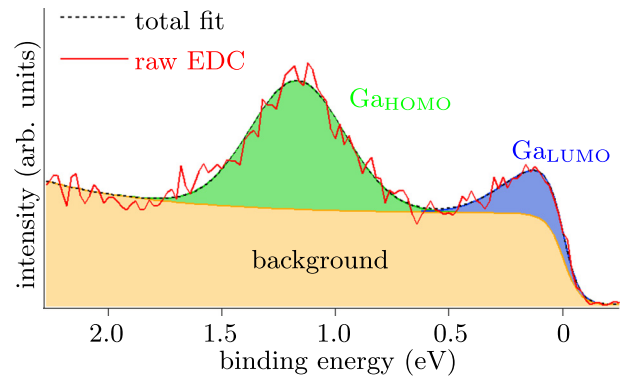

FIG. 7. Example of the applied fitting routine. EDC taken of the 40 eV ML data at $(k_x/k_y) = (1.2/-0.6)$ 1/Å. The yellow area marks the background from the substrate and in green/blue the area of the fitted Gaussian of the HOMO/LUMO is shown, which were used to build the fitted momentum maps presented above.

the data in a particular color code. In Fig. 6, we explain the background treatment exemplary on the momentum map of the ML HOMO with an excitation energy of $h\nu = 40\,\mathrm{eV}$. Figure 6(a) shows the measured HOMO in the standard color code as used so far. By applying the fitting routine, which is already described above and exemplified in Fig. 7 to every EDC of the 3D data set at each point in $k_{||}$, we are able to separate the molecular signal from the substrate by plotting the area of the fitted Gaussian (green or blue areas of Fig. 7) of the corresponding molecular orbital. The result of this procedure is shown in Fig. 6(b), also with the standard color code. Figures 6(c) and 6(d) present the same data as in Figs. 6(a) and 6(b) but with a color scale such that the low-intensity signal is fully shown. By comparing Figs. 6(a) and 6(c), one can recognize that, due to the color code, most of the background's intensity can already be suppressed, in this case just the Ag-bands on the right side, which are most intense due to the experimental geometry, are slightly visible in Fig. 6(a). This structured intensity is what the fitting routine is able to filter for the most part as can be seen in Fig. 6(d). Here almost all of the structured background is excluded and only the molecular signal and the unstructured background remain. By now, applying the standard color scale, the inelastic background from the substrate is successfully reduced and the molecular pattern remains [see Fig. 6(b)]. Determining the molecular tilt angle without background treatment is only possible within a reasonable error bar for low excitation energies up to $h\nu \approx 30 - 40\,\mathrm{eV}$, due to the much higher cross section of the carbon-containing molecules and, therefore, lower influence impact of the substrate. At higher excitation energies, a thorough background treatment is mandatory.

Figure 6(e) shows the momentum map of the clean Ag(110) substrate at the same energy as Figs. 6(a)– 6(d), which can also be recognized as background in Fig. 6(C). Here the only difference is the experimental geometry with the incoming light from the bottom, which instead of producing a left/right asymmetry as in all the other maps presented so far, results in a slight top/bottom difference. The overall trend of the sp-bands for comparison is nevertheless clearly visible.

[1] T.-C. Tseng, C. Urban, Y. Wang, R. Otero, S. L. Tait, M. Alcamí, D. Écija, M. Trelka, J. M. Gallego, N. Lin *et al.*, Nat. Chem. **2**, 374 (2010).

[2] J. Hwang, A. Wan, and A. Kahn, Mater. Sci. Eng. R **64**, 1 (2009).

[3] O. L. Monti, J. Phys. Chem. Lett. **3**, 2342 (2012).

[4] H. Ishii, K. Sugiyama, E. Ito, and K. Seki, Adv. Mater. **11**, 605 (1999).

[5] S. Braun, W. R. Salaneck, and M. Fahlman, Adv. Mater. **21**, 1450 (2009).

[6] A. Kahn, N. Koch, and W. Gao, J. Polym. Sci., Part B: Polym. Phys. **41**, 2529 (2003).

[7] A. Schöll and F. Schreiber, in *Molecular Beam Epitaxy* (Elsevier, Amsterdam, New York, 2013), pp. 591–609.

[8] S. R. Forrest, Chem. Rev. **97**, 1793 (1997).

[9] S. Duhm, G. Heimel, I. Salzmann, H. Glowatzki, R. L. Johnson, A. Vollmer, J. P. Rabe, and N. Koch, Nat. Mater. **7**, 326 (2008).

[10] W. R. Salaneck, K. Seki, A. Kahn, and J.-J. Pireaux, *Conjugated Polymer and Molecular Interfaces: Science and Technology for Photonic and Optoelectronic Application* (CRC Press, Basel, New York, 2001).

[11] C. M. Schneider, C. Wiemann, M. Patt, V. Feyer, L. Plucinski, I. Krug, M. Escher, N. Weber, M. Merkel, O. Renault *et al.*, J. Electron Spectrosc. Relat. Phenom. **185**, 330 (2012).

[12] Y. Wang, W. Ji, D. Shi, S. Du, C. Seidel, Y. Ma, H.-J. Gao, L. Chi, and H. Fuchs, Phys. Rev. B **69**, 075408 (2004).

[13] J. Ziroff, F. Forster, A. Schöll, P. Puschnig, and F. Reinert, Phys. Rev. Lett. **104**, 233004 (2010).

[14] Y. Zou, L. Kilian, A. Schöll, T. Schmidt, R. Fink, and E. Umbach, Surf. Sci. **600**, 1240 (2006).

[15] M. Wießner, J. Ziroff, F. Forster, M. Arita, K. Shimada, P. Puschnig, A. Schöll, and F. Reinert, Nat. Commun. **4**, 1514 (2013).

[16] T. Permien, R. Engelhardt, C. Feldmann, and E. Koch, Angle-Resolved Photoemission from Oriented Films of Lead Phthalocyanine on a Cu (100) Surface, No. DESY-SR–83-06, Deutsches Elektronen-Synchrotron (DESY), 1983.

[17] C. Tusche, A. Krasyuk, and J. Kirschner, Ultramicroscopy **159**, 520 (2015).

[18] N. Barrett, J. Rault, J. Wang, C. Mathieu, A. Locatelli, T. Mentes, M. Nino, S. Fusil, M. Bibes, A. Barthélémy *et al.*, J. Appl. Phys. **113**, 187217 (2013).

[19] C. Mathieu, N. Barrett, J. Rault, Y. Mi, B. Zhang, W. De Heer, C. Berger, E. Conrad, and O. Renault, Phys. Rev. B **83**, 235436 (2011).

[20] A. Liebsch, Phys. Rev. B **13**, 544 (1976).

[21] T. Fujikawa and H. Arai, J. Electron Spectrosc. Relat. Phenom. **123**, 19 (2002).

[22] S. Hasegawa, S. Tanaka, Y. Yamashita, H. Inokuchi, H. Fujimoto, K. Kamiya, K. Seki, and N. Ueno, Phys. Rev. B **48**, 2596 (1993).

[23] M. Frisch, G. Trucks, H. Schlegel, G. Scuseria, M. Robb, J. Cheeseman, G. Scalmani, V. Barone, B. Mennucci, G. Petersson *et al.*, Gaussian 09, revision A. 1. (Gaussian Inc., Wallingford, CT, 2009), Vol. 27, p. 34.

[24] A. D. Becke, J. Chem. Phys. **98**, 5648 (1993).

[25] C. Lee, W. Yang, and R. G. Parr, Phys. Rev. B **37**, 785 (1988).

[26] N. Ueno, K. Suzuki, S. Hasegawa, K. Kamiya, K. Seki, and H. Inokuchi, J. Chem. Phys. **99**, 7169 (1993).

[27] E. Reinisch, P. Puschnig, T. Ules, M. Ramsey, and G. Koller, Phys. Rev. B **93**, 155438 (2016).

[28] N. Ueno, A. Kitamura, K. K. Okudaira, T. Miyamae, Y. Harada, S. Hasegawa, H. Ishii, H. Inokuchi, T. Fujikawa, T. Miyazaki *et al.*, J. Chem. Phys. **107**, 2079 (1997).

[29] M. Dauth, M. Graus, I. Schelter, M. Wießner, A. Schöll, F. Reinert, and S. Kümmel, Phys. Rev. Lett. **117**, 183001 (2016).

[30] P. Puschnig, S. Berkebile, A. J. Fleming, G. Koller, K. Emtsev, T. Seyller, J. D. Riley, C. Ambrosch-Draxl, F. P. Netzer, and M. G. Ramsey, Science **326**, 702 (2009).

[31] S. Söhnchen, S. Lukas, and G. Witte, J. Chem. Phys. **121**, 525 (2004).

[32] M. Graus, M. Grimm, C. Metzger, M. Dauth, C. Tusche, J. Kirschner, S. Kümmel, A. Schöll, and F. Reinert, Phys. Rev. Lett. **116**, 147601 (2016).

[33] S. Weiß, D. Lüftner, T. Ules, E. Reinisch, H. Kaser, A. Gottwald, M. Richter, S. Soubatch, G. Koller, M. Ramsey *et al.*, Nat. Commun. **6**, 8287 (2015).

[34] J.-J. Yeh, *Atomic Calculation of Photoionization Cross-Sections and Asymmetry Parameters* (Gordon & Breach Science Publ.; AT&T Bell Laboratories, 1993).

[35] J. J. Yeh and I. Lindau, At. Data Nucl. Data Tables **32**, 1 (1985).

[36] T. Breuer, M. Klues, and G. Witte, J. Electron Spectrosc. Relat. Phenom. **204**, 102 (2015).

[37] J. Smerdon, M. Bode, N. Guisinger, and J. Guest, Phys. Rev. B **84**, 165436 (2011).